

E. A. Ervin
Assistant Professor,
Department of Mechanical and
Aerospace Engineering,
The University of Dayton,
Dayton, OH 45469

G. Tryggvason
Associate Professor,
Department of Mechanical Engineering and
Applied Mechanics,
The University of Michigan,
Ann Arbor, MI 48109

The Rise of Bubbles in a Vertical Shear Flow

Full numerical simulations of two- and three-dimensional bubbles in a shear flow, by a finite difference front tracking method, are presented. The effects of inertial, viscous, gravitational, and surface forces on the lift of a deformable bubble rising due to buoyancy in a vertical shear flow, are examined. Bubbles with a large surface tension coefficient migrate toward the downward moving fluid, as predicted analytically for a cylinder or a sphere in a shear flow. Bubbles with smaller surface tension deform, and generally migrate in the opposite direction. The combined effects of the shear flow and the buoyancy deform the bubble in such a way that the circulation around the deformed bubbles is opposite to that of undeformed bubbles.

Introduction

Bubbles in shear flows are of underlying importance in many processes. While it is often the collective behavior of many bubbles that is of most engineering relevance, rather than the motion of individual bubbles, the global properties of a multiphase flow are usually determined by the smallest scales in the flow. The coupling of the bubble motion to that of the outer liquid flow is central to understanding the dynamics of bubbles. While a number of studies have focused on the drag on bubbles, the lift is poorly understood. Although a body of literature is available for rigid particles, the effect of deformation has received little attention.

A spinning body in translational motion will experience a force in a direction perpendicular to both the direction of motion and the rotation axis. As shown in Fig. 1, the nonuniform fluid flow causes the particle to rotate, resulting in a force in the y -direction:

$$\mathbf{F} = \beta \rho_2 V (\boldsymbol{\omega} \times \mathbf{U}_{P/F}). \quad (1)$$

Here, $|\boldsymbol{\omega}|$ is equal to the velocity gradient, G , which is taken to be constant far from the particle (Fig. 1), and $\mathbf{U}_{P/F}$ is the relative velocity of the particle with respect to the fluid. For inviscid flow around a rigid two-dimensional cylinder, β is 2.0 and V is the cross-sectional area, πa^2 (Batchelor, 1967). For inviscid flow around a rigid sphere, β is 0.5 and V is the sphere volume (Auton, 1988). The resulting lift force on the particle, also known as the Magnus effect, causes lateral migration across the streamlines of the outer flow in the direction of \mathbf{F} .

Bretherton (1962) examined the migration of nonspherical rigid particles in a shear flow where the shear Reynolds number, G_R , is very small. Saffman (1965) examined the lift of a sphere in a shear flow where G_R , and the slip Reynolds number, Re , are both small, showing that the lift force is:

$$\mathbf{F} = -6.46 a^2 |\mathbf{U}_{P/F}| \sqrt{\rho_1 \mu_1 |G|} \text{sign}(G). \quad (2)$$

McLaughlin (1991, 1993) extended the range of G_R relative to Re , and included the effect of a nearby wall. Dandy and Dwyer (1990) numerically examined a fixed sphere in a shear flow at finite Re . They used a body fitted grid and a finite volume method and found that the lift force is proportional to the shear rate and the square of the fluid velocity. Recent experimental studies by Sridhar and Katz (1995), of very small spherical bubbles interacting with a vortex, showed a similar trend as predicted by the various theoretical models. Their experiments

were carried out under different conditions than those for which the theories were valid, and therefore yielded considerable quantitative differences in the results. However, the differences show the sensitivity of the lift force on a rigid body to the competing influences of inertial, viscous, and gravitational forces, and illustrate the incomplete state of the knowledge about lift on bubbles in shear flows.

In addition to inertia, other factors such as wall proximity, nonsphericity and non-Newtonian fluid properties, shear gradients and deformability can influence the motion of particles, as described by Leal (1980). Asymmetric deformation, in particular, causes the particle to migrate laterally to an equilibrium position. Quantifiable observations of the lateral migration of neutrally buoyant drops in shear flow were first made by Goldsmith and Mason (1962) and by Karnis and Mason (1967). Duplication of the experiments with a solid particle showed no lateral migration, indicating that the migration is deformation induced. Models of this phenomenon have assumed Stokes flow (for example, Uijttewaal et al., 1993). Simulations of a deformable particle in shear flow have generally been limited to droplets with minute G_R in an infinite flow regime with no relative motion (Rallison, 1984). More recent studies have included walls or finite G_R (for example, Zhou and Pozrikidis, 1993 and Kang and Leal, 1987, 1989). No attempt appears to have been made to model a deformable particle in inertia-induced motion.

Kariyasaki (1987) performed an experiment releasing both deformable and solid bodies in a simple vertical shear flow generated by a belt driven mechanism in a fluid filled tank. Both solid particles and liquid droplets were introduced at the top of the tank and both were observed to migrate laterally toward one of the belts. However, measured displacement traces of the particles showed that the direction of migration of the droplets was opposite to that of the solid particles. Kariyasaki also released gas bubbles at the bottom of the tank. The bubbles rose due to buoyancy and again, drifted in a direction opposite to that expected from the theoretical predictions for a solid particle. Although the deformation was not quantified, the bubbles and drops were highly deformed.

The objective of this study is to gain insight into the fundamental behavior of bubbles rising in a simple shear flow by full numerical simulation of the Navier-Stokes equations. The physical problem is defined and the numerical technique is outlined briefly in the next section. The following sections show a number of two-dimensional results to explain the basic mechanisms and their dependency on the governing parameters of the flow. Finally, it is shown that three-dimensional simulations confirm the two-dimensional predictions.

Numerical Procedure

The front-tracking method consists of a finite difference approximation of the full Navier-Stokes equations with explicit

Contributed by the Fluids Engineering Division for publication in the JOURNAL OF FLUIDS ENGINEERING. Manuscript received by the Fluids Engineering Division December 25, 1994; revised manuscript received September 4, 1996. Associate Technical Editor: R. W. Metcalfe.

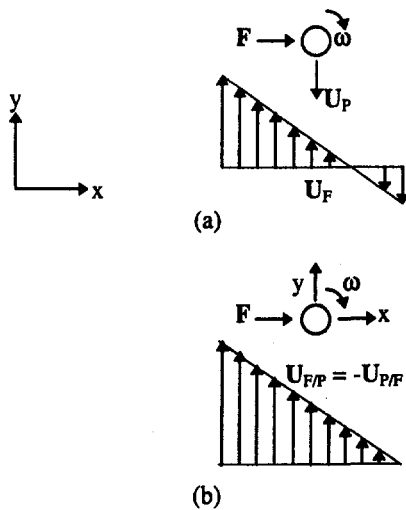


Fig. 1 Schematic of particle force due to relative motion in a nonuniform flow (a) viewed from an external frame of reference (b) viewed from the particle

tracking of a distinct free boundary at the interface between the bubble and the ambient fluid. Unverdi and Tryggvason (1992a) introduced the method to track one or more bubbles rising through a quiescent flow, and they numerically simulated both two- and three-dimensional rising bubbles (Unverdi and Tryggvason, 1992a, 1992b). The method is described below.

The Navier-Stokes equations govern the fluid motion both inside and outside the bubbles and a single vector equation can be written for the whole flow field. In conservative form:

$$\frac{\partial \rho \mathbf{U}}{\partial t} + \nabla \cdot \rho (\mathbf{U} \otimes \mathbf{U}) = -\nabla p + (\rho_o - \rho) \mathbf{g} + \nabla \cdot \mu [(\nabla \otimes \mathbf{U}) + (\nabla \otimes \mathbf{U})^T] - \int_{\text{Front}} \kappa'_f \mathbf{n}'_f \delta^i(\mathbf{x} - \mathbf{x}'_f) dA'_f \quad (3)$$

where \otimes denotes the tensor product of two vectors. Surface forces are added at the interface between the bubbles and the ambient fluid. δ^i is a two or three-dimensional delta function obtained by multiplying together one-dimensional delta functions. The dimension is denoted by $i = 2$ or 3 . κ_f is the curvature for two-dimensional flow and twice the mean curvature for three-dimensional flows. Formally, the integral is over the entire front, thereby adding the delta functions together to create a force that is concentrated at the interface, but smooth along the surface of the bubbles. The primed variables are evaluated at \mathbf{x}_f , the front position. In the actual numerical code, the integral is evaluated only for points close to the front.

The mass conservation equation can be written:

$$\frac{D\rho}{Dt} + \rho \nabla \cdot \mathbf{U} = 0 \quad (4)$$

where $D()/Dt$ is the material derivative. The equations of state for the density and viscosity:

$$\frac{D\rho}{Dt} = 0 \quad (5)$$

$$\frac{D\mu}{Dt} = 0 \quad (6)$$

simply state that density and viscosity within each fluid remain constant. Equations (4) and (5) can therefore be combined:

$$\nabla \cdot \mathbf{U} = 0 \quad (7)$$

for the entire domain, which, when combined with the momentum equations leads to a nonseparable elliptic equation for the pressure.

These equations implicitly enforce the proper stress conditions at the fluid interface. If we integrate Eq. (3) over a small volume containing the interface, most of the terms go to zero in the limit of infinitesimal volume, resulting in:

$$\{-p\mathbf{n} + \mu\mathbf{n} \cdot [(\nabla \otimes \mathbf{U}) + (\nabla \otimes \mathbf{U})^T]\} = \sigma \kappa'_f \mathbf{n} \quad (8)$$

where the outer braces denote the jump across the interface. This is, of course, the usual statement of continuity of stresses

Nomenclature

A = surface area
 a = radius of undeformed bubble
 A_p = projected area ($A_p = 2a$ for 2D bubble)
 d = diameter of undeformed bubble
 C = lift force coefficient, $C = 2|\mathbf{F}| \text{sign}(\mathbf{F})/(\rho_1 v_{P/F}^2 A_p)$
 Ca = capillary number, $Ca = Ga\mu_1/\sigma$
 D = deformation, $(1 - E)/(1 + E)$
 E = ellipse ratio: minor axis to major axis
 \mathbf{F} = lift force, $\mathbf{F} = \beta \rho_2 V (\omega \times \mathbf{U}_{P/F})$
 Fr = Froude number, $Fr^2 = G^2 a/g$
 fx = lift force in x direction
 G = velocity gradient, $G = \partial v/\partial x = 2U_o/l$
 G_R = Reynolds number calculated using G , $G_R = \rho_1 G d^2/\mu_1$
 \mathbf{g} = gravitational acceleration vector
 l = distance between sheared walls
 \mathbf{n}_f = unit vector normal to bubble surface, pointing out
 p = fluctuating pressure

Re = Reynolds number calculated with $v_{P/F}$, $Re = \rho_1 v_{P/F} d/\mu_1$
 t = time
 \mathbf{U} = velocity vector
 U_o = nominal velocity of sheared wall
 v = velocity component in vertical direction
 V = volume (3-D)
 We = Weber number, $We = \rho_1 G^2 a^3/\sigma$
 \mathbf{x} = position vector
 x, y, z = cartesian coordinates (bubble centroid)

Superscripts

i = flow dimension index

Subscripts

1 = fluid material property
 2 = bubble or drop material property
 D = drag force

F = fluid (vector)
 f = bubble front
 P = particle vector
 P/F = particle vector relative to fluid vector

Greek

α = finite shear rate, $\alpha = 0.5 * G/v_{P/F} = 0.5 * G_R/Re$
 β = coefficient for lift force, \mathbf{F}
 Γ = circulation, cm^2/s
 δ = delta function, $\delta(0) = 1$
 θ = angle between the path and the vertical axis
 η = density ratio, $\eta = \rho_2/\rho_1$
 κ = twice the average front curvature (3-D)
 λ = viscosity ratio, $\lambda = \mu_2/\mu_1$
 μ = dynamic viscosity
 ρ = density
 ρ_o = density of an equivalent homogeneous system
 σ = surface tension
 ω = vorticity vector

at a fluid boundary, showing that the tangential stresses are continuous and that the normal stresses are balanced by surface tension. Integrating the mass conservation Eq. (4) across the interface shows that the continuity of the normal velocities is also satisfied.

A finite difference discretization of the above equations advances the flow field over a staggered mesh while additional computational elements explicitly track the interface between the two fluids. Since the fluids are incompressible, the front motion is determined solely from the velocity field that is interpolated from the grid. The tracked interface carries the jump in fluid properties that are distributed onto the grid to reconstruct the density or viscosity fields. The separation between the two fluids is not completely abrupt but has a finite thickness on the order of a grid spacing. This thickness remains constant, as there is no numerical diffusion, and provides stability and smoothness to the solution. The thickness does, however, depend on the size of the grid used; in the limit of infinitely high resolution, the thickness goes to zero. As shown later in the paper, the resolution tests demonstrate that the solution converges relatively fast under grid refinement. The tracked interface locates the surface tension forces and the interface position provides the basis to update the density and viscosity fields. To keep the elements at an optimum size and shape, it is imperative to reconfigure the interface at each time step, particularly in the case of the three-dimensional surfaces. The present study used a version of the numerical method that is second order both in time and space. The time step is automatically updated at each time step to ensure stability. The calculations were performed in double precision on a work station, or on a Cray Y-MP that uses a 64-bit word making single precision equivalent to double precision on a 32-bit machine. Further details of the code and its verification are given in Ervin (1993).

The problem is described in Fig. 2. Assume that an initially spherical bubble with radius a , density ρ_2 , viscosity μ_2 , and surface tension coefficient σ is suspended in a fluid of density ρ_1 , and viscosity μ_1 . The region is bounded in the x -direction by rigid walls moving in opposite directions with a constant velocity U_o . The boundaries are periodic in the other two directions. In the case of the two-dimensional models, the bubble is initially a cylinder. Gravity acts in the negative y -direction,

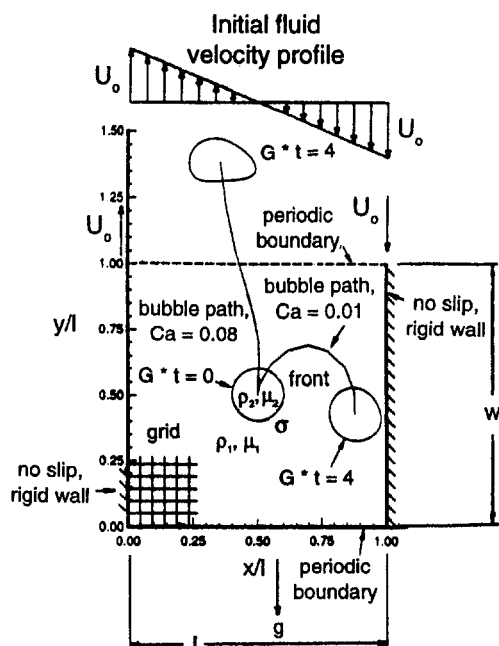


Fig. 2 Effect of Ca on bubble motion. $G_R = 16.0$, $Fr^2 = 0.20$, $\eta = 0.025$, $\lambda = 0.10$, and $a/l = 0.10$.

resulting in motion of the bubble, relative to the suspending fluid. Along with the viscosity and density ratios, λ and η , respectively, and the ratio a/l , the three-independent dimensionless groups that define the problem are the shear Reynolds number, $G_R = \rho_1 G d^2 / \mu_1$, the Froude number squared, $Fr^2 = G^2 a / g$, and the capillary number, $Ca = G a \mu_1 / \sigma$ (alternatively, the Weber number, $We = \rho_1 G^2 a^3 / \sigma$). Position and size are scaled by l , deformation by a , velocity by U_o , time by G , and stress by μG . Here, the width of the periodic domain is equal to l .

For the results presented in the following sections, the density ratio is $\eta = 0.025$. While the intent was to simulate a gas bubble in water, previous studies by Unverdi and Tryggvason (1992a) have shown that decreasing η further did not have such a significant effect on the results that it warranted the ensuing computational cost. Also, the ratio of dynamic viscosity is of the order of 10, thus $\lambda = 0.10$. The bubble is released at time zero into an initially linear velocity field (Couette flow) from a position centered in the periodic directions (y/l or z/l is 0.5) while the initial x/l varies.

Results and Discussion

This section presents numerical simulations of buoyant deformable bubbles in a linear vertical shear flow. Beginning with a two-dimensional model, the effects of deformation of sheared bubbles on circulation, migration and lift are investigated. More realistic three-dimensional bubbles are then considered.

Effect of Deformation on Migration. In this section, the effect of Ca on bubble deformation and migration is analyzed with constant G_R and Fr^2 . Figure 2 shows the effect of deformation on two bubbles with $G_R = 16.0$, $Fr^2 = 0.20$, and $a/l = 0.1$, initially at $x/l = 0.500$, computed on a 128 by 128 grid. The bubble contours are plotted at time $G^*t = 4$, along with their path. The bubble with the greatest surface tension ($Ca = 0.01$) remained fairly cylindrical. It initially rose in the positive y -direction, but then migrated toward the wall that moved in the negative y -direction, and eventually turned in the negative y -direction. The bubble migration was in the direction of the lift force, F (Eq. (1)), due to the clockwise rotation induced by the sheared walls and the upward relative motion of the bubble. In contrast, the bubble with a lower surface tension coefficient ($Ca = 0.08$) developed an inverted tear drop shape. It rose and then migrated toward the upward moving wall in a manner similar to the deformed bubbles and drops described by Kariyasaki (1987).

Figure 3 shows the path of the two-dimensional bubbles resolved on 32^2 , 64^2 , and 128^2 grids. The bubble fronts for $Ca = 0.01$ are plotted at time $G^*t = 1.5$ (Fig. 3(a)) and for $Ca = 0.08$ at $G^*t = 3.0$ (Fig. 3(b)). While all runs show similar behavior, the exact path of the coarsely resolved bubble differs somewhat from the better resolved ones, and its shape has large irregularities on the bottom ($Ca = 0.08$). The bubble with 64^2 grid resolution has slight irregularities on the bottom, but the shape is nearly identical to the best resolved bubble. The latter moves slightly faster than the former, so that if we wait long enough, the actual positions will be different although the paths are nearly identical. The size of the bubble, a/l , was based on a preliminary study to reduce wall effects while allowing the bubble to develop a sufficient Re . The cross-sectional area of the bubble was calculated using Stokes' theorem at each time step as a check on the solution, with satisfying results.

The following set of figures examine the bubbles described in Fig. 2. The initially cylindrical bubbles were released from a noncentered x -value. This was to examine each bubble after any changes to its shape and migration by the time the bubble reached the center of the flow domain, with reduced wall effects. The bubble with $Ca = 0.01$ started from $x/l = 0.175$ and continuously migrated in the positive x -direction as before, until it

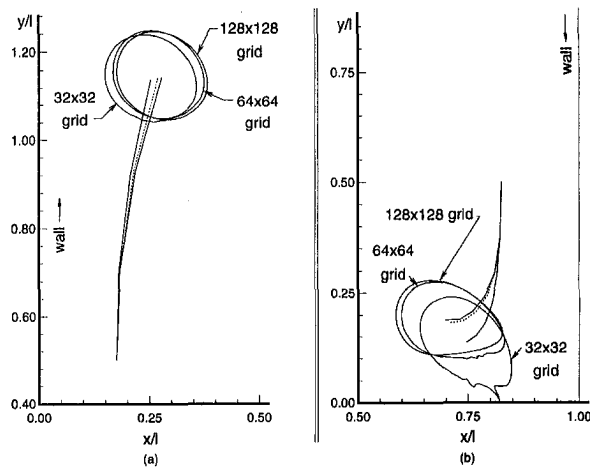


Fig. 3 Effect of grid resolution on a two-dimensional bubble. $G_R = 16.0$, $Fr^2 = 0.20$, $\eta = 0.025$, $\lambda = 0.10$ and $a/l = 0.10$. (a) $Ca = 0.01$ and $G^*t = 1.5$, (b) $Ca = 0.08$ and $G^*t = 3.0$.

encountered the wall. The deformed bubble, $Ca = 0.08$, started from $x/l = 0.825$ and migrated in the negative x -direction, as when it was released midway between the walls. Since this bubble started out near the wall moving in the negative y -direction, it moved in the negative y -direction before buoyancy had a significant effect.

Figure 4 shows the flow field as seen from a coordinate frame moving with the individual bubble centroids, at a time when each bubble solution has reached a steady shape (no further deformation) in the center of the flow region. This occurred at $G^*t = 3.0$ for the cylindrical bubble ($Ca = 0.01$, Fig. 4(a)), and at $G^*t = 7.0$ for the low surface tension bubble ($Ca = 0.08$, Fig. 4(b)). Velocity vectors and streamlines are shown with respect to the bubble frame of reference, and the velocity unit shown in the figures represents the velocity of the wall. The bubble front is overlaid on the velocity field. The steady shape of each bubble was a distorted ellipse, with the minor axis aligned with the direction of the bubble motion. The side of the bubble approaching the respective wall had a higher radius of curvature. This was especially pronounced for the bubble with $Ca = 0.08$. The internal flow within a bubble rising in a quiescent flow generally consists of two vortices of equal strength but opposite circulation, driven by flow past the bubble. Since the bubbles of Fig. 4 are rising with respect to the flow, such vortices are expected. Furthermore, the vortex on the side that has larger relative motion should be stronger, and this is exactly what is observed. The predominant vortex in the round bubble ($Ca = 0.01$, Fig. 4(a)) rotated in the clockwise direction required by the outer shear flow, and was located in the side of the bubble facing the downward moving wall. In the case of the high Ca bubble, the vortex in the side facing the upward moving wall was the larger of the two and rotated in the counter-clockwise direction. The clockwise vortex filled the smaller end of the bubble.

Figure 5 shows the bubble circulation ($\Gamma/U_o/l$) as a function of time for each of the two bubbles of Fig. 4. From the sheared walls, the bubble circulation was expected to be negative (clockwise). This was the case, initially, when both bubbles were fairly cylindrical. However, the deformed bubble quickly began to shift to a positive circulation. Thus it appears that the counter-clockwise vortex seen in Fig. 4(b) dominated the overall circulation of the deformed bubble. This result confirms the lift acceleration effect: the unexpected migration direction of the deformed bubble is due to a counter-clockwise circulation. Interestingly, the circulation of the cylindrical bubble also increased under the influence of the wall, suggesting that both

wall and deformation influence the lift acceleration and the bubble migration.

Parametric Study of Lift. A parametric study evaluated the effect of varying G_R , Fr^2 , and Ca on bubble lift force and deformation, at $a/l = 0.1$. These parameters, especially Ca , were selected to be in the critical range where the lift force changes direction. G_R and Fr^2 , particularly the latter, were limited by computational requirements. The lift force was calculated by applying a force on the bubble to hold it centered between the two walls. Figure 6 presents the lift force coefficient, C_{fx} , as a function of Ca , for four combinations of G_R and Fr^2 . One of the curves corresponds to $G_R = 16.0$ and $Fr^2 = 0.20$, as in the previous section. The bubble with a high surface tension ($Ca = 0.01$) had a positive C_{fx} , toward the downward moving wall. This was comparable to a solid cylindrical parti-

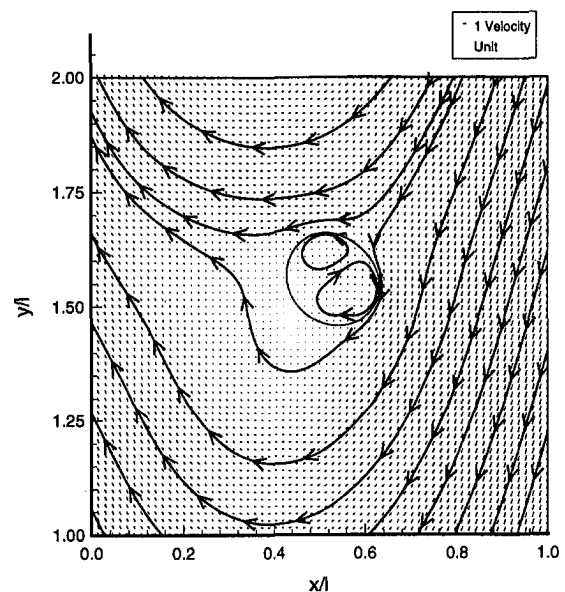


Fig. 4(a)

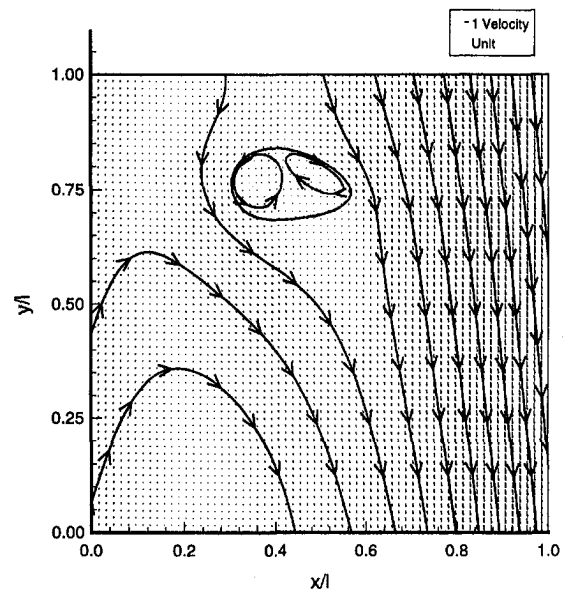


Fig. 4(b)

Fig. 4 Velocity field with respect to the centroid of a steady bubble. $G_R = 16.0$, $Fr^2 = 0.20$, $\eta = 0.025$, $\lambda = 0.10$ and $a/l = 0.10$. (a) $Ca = 0.01$, $G^*t = 3$ and initial $x/l = 0.175$, (b) $Ca = 0.08$, $G^*t = 7$ and initial $x/l = 0.825$.

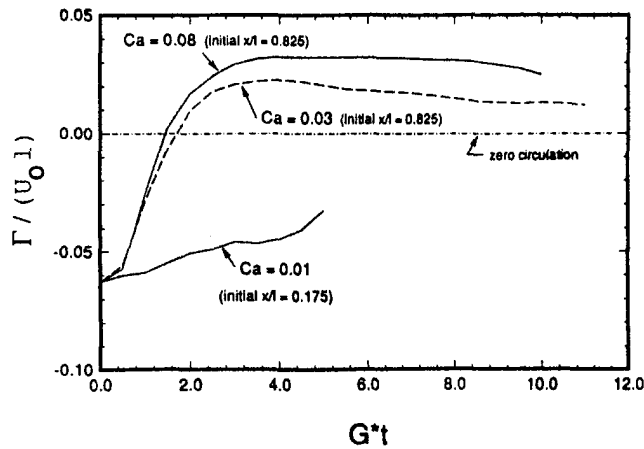


Fig. 5 Bubble circulation (Γ/U_0l) as a function of time. $G_R = 16.0$, $Fr^2 = 0.20$, $\eta = 0.025$, $\lambda = 0.10$ and $a/l = 0.10$.

cle, as expected due to the tendency of a low Ca bubble not to deform. Increasing Ca resulted in a negative lift force, toward the upward moving wall. This agrees with the results of Fig. 2. The consequence of reducing the shear Reynolds number ($G_R = 8.0$) was to increase C_{fx} in the positive x -direction. These bubbles behaved more as solid cylindrical particles even at higher Ca . Reducing Fr^2 to a value of 0.18, however, increased C_{fx} in the negative x -direction.

The lift coefficient of the low Ca cylindrical bubble at $G_R = 8$, $Fr^2 = 0.2$ is 2.0. This is similar to the theoretical lift coefficient of 1.3 for a buoyant rigid sphere in low Re flow, from Eq. (2) (Saffman, 1965). The Re for this bubble is 9.0, and the corresponding calculated drag coefficient is 3.0, which corresponds very well to experimental results for solid cylinders (Schlichting, 1979). However, this result must be somewhat fortuitous: the expected lower friction drag on the bubble is apparently offset by increased drag due to wall effects.

The lift force results can be considered further by looking at the bubble deformation (Fig. 7), where D is defined as:

$$D = (1 - E)/(1 + E). \quad (9)$$

Here, E is the ratio of the minor to major axes of an ellipse. E was calculated by equating the area moments of inertia of the bubble, as tracked by the front, to those of an ellipse. Again, one of the curves corresponds to $G_R = 16.0$ and $Fr^2 = 0.20$. The bubble with $Ca = 0.01$ had a low deformation ($D = 0.0844$) which explains why a positive lift force accelerated it like a

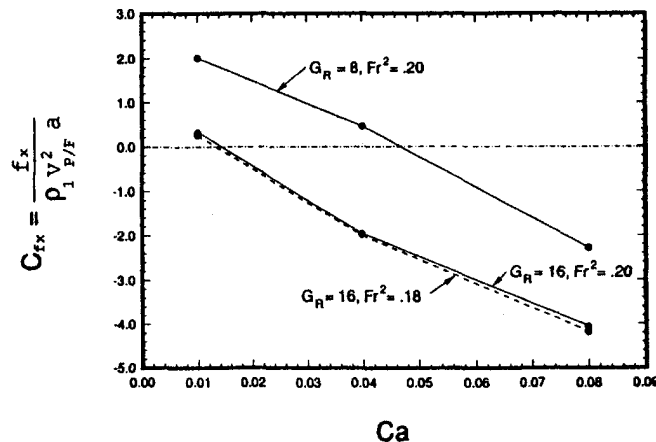


Fig. 6 Variation of lift force coefficient (C_L) with Ca . $\eta = 0.025$, $\lambda = 0.10$ and $a/l = 0.10$.

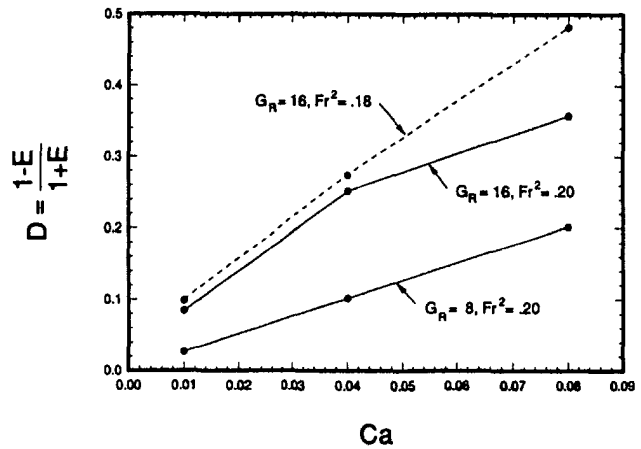


Fig. 7 Variation of deformation (D) with Ca . $\eta = 0.025$, $\lambda = 0.10$ and $a/l = 0.10$.

solid cylindrical particle. Lower surface tension increased D and thus increased the deformation induced lift force in the negative x -direction. Decreasing the relative influence of inertia ($G_R = 8.0$), decreased both D and the negative lift that is caused by deformation. A decreased Froude number ($Fr^2 = 0.18$) increased the deformation. The larger terminal velocity associated with a lower Fr may have contributed to the negative lift force as well as any deformation induced circulation.

Three-Dimensional Calculations. Simulations of two three-dimensional bubbles at $G_R = 16.0$, $Fr^2 = 0.15$ and $a/l = 0.15$ are now considered. Preliminary studies revealed that the three-dimensional bubbles migrated more slowly than their two-dimensional counterparts. Slower migration of the three-dimensional bubbles might be expected from examination of Eq. (1) where β is 0.5 for a sphere and 2 for a two-dimensional cylinder. Thus, a lower Fr was selected than that of the two-dimensional bubbles described earlier.

Due to the memory limits of the Cray Y-MP, a 64^3 grid was used. The bubble size, a/l , was increased for greater resolution within the bubble than would be obtained with a smaller bubble at this grid density. We repeated the 64^3 simulations on a 32^3 grid and found that the behavior is similar, though the results are not identical. Figure 8 shows the bubble path for both resolutions with the bubble shapes at $G^*t = 3.6$ for $Ca = 0.01$ (Fig. 8(a)) and at $G^*t = 2.4$ for $Ca = 0.07$ (Fig. 8(b)). While the computation was not repeated on a grid finer than 64^3 , a more extensive resolution study in two-dimensions was performed

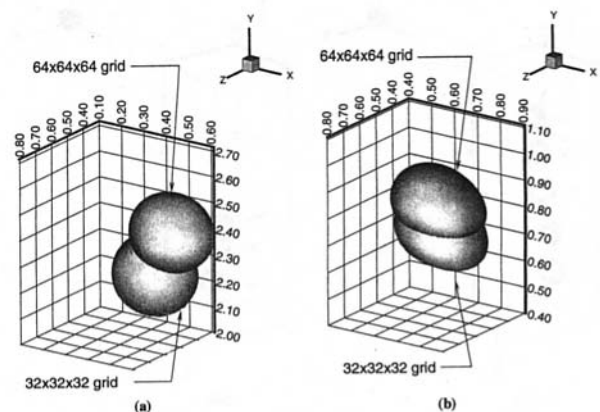


Fig. 8 Effect of grid resolution on a three-dimensional bubble. $G_R = 16.0$, $Fr^2 = 0.15$, $\eta = 0.025$, $\lambda = 0.10$ and $a/l = 0.15$. (a) $Ca = 0.01$ and $G^*t = 3.6$, (b) $Ca = 0.07$ and $G^*t = 2.4$.

(Fig. 3). By comparing the three-dimensional and the two-dimensional results on the 32^2 and the 64^2 grids, the convergence rates are seen to be very comparable. Since the 128^2 grid results in two-dimensions suggest that the 64^2 grid results are nearly fully converged, we believe that the same is true for the three-dimensional results, especially with the increased bubble size.

A bubble with $Ca = 0.01$ was started at $x/l = 0.175$ (Fig. 9(a)), near the upward moving wall, and another bubble with $Ca = 0.07$ was put at $x/l = 0.825$ (Fig. 9(b)). As in the case of the two-dimensional bubbles, the two three-dimensional bubbles were released near one of the walls so that the flow field and the bubble would have sufficient time to adjust to one another by the time the bubble moved to the center of the channel.

Figure 9(a) shows the low Ca bubble ($Ca = 0.01$) at five moments in time. The bubble deformed little and migrated toward the downward moving wall, as anticipated. After an initial start-up period, the bubble moved at a constant rate upwards and in the positive x -direction. Due to the relatively high terminal velocity of the bubble, it is anticipated that it would continue to move upward and eventually reach a steady x -value due to the influence of the downward moving wall. The bubble shape and motion were steady by $G^*t = 1.8$.

The bubble with $Ca = 0.07$ is shown in Fig. 9(b). This bubble deformed into an egg-like shape and migrated in the negative x -direction as it rose, like the two-dimensional bubble with $Ca = 0.08$. Though not apparent from Fig. 9(b), the bubble moved in the negative y -direction a very small distance before buoyancy had a significant effect, due to its initial location in the negative shear regime. The bubble moved at a constant rate and maintained a constant shape after $G^*t = 2.7$.

Figure 10 examines the flow field at a time when the individual bubbles were steady in terms of the deformation and flow field, and when the bubbles had moved away from the walls, at $G^*t = 3.6$. These figures depict the flow field with velocity vectors, as seen from a frame of reference moving with bubble centroid, in the x - y plane perpendicular to the walls through the bubble centroid ($z/l = 0.50$). The bubble front is overlaid on the velocity field. The flow field of the nearly spherical bubble ($Ca = 0.01$) is illustrated in Fig. 10(a). A counter-clockwise vortex is present in the left-hand side of the bubble, and a stronger clockwise vortex is seen to the right of the counter-clockwise vortex. The velocity field of the deformed bubble ($Ca = 0.07$) is shown in Fig. 10(b). A counter-clockwise vortex is located in the left-hand side of the bubble, and a weaker clockwise vortex is seen in the right-hand side of the bubble. The

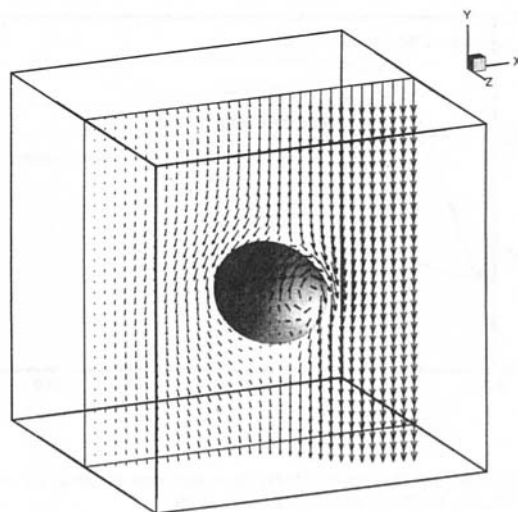


Fig. 10(a)

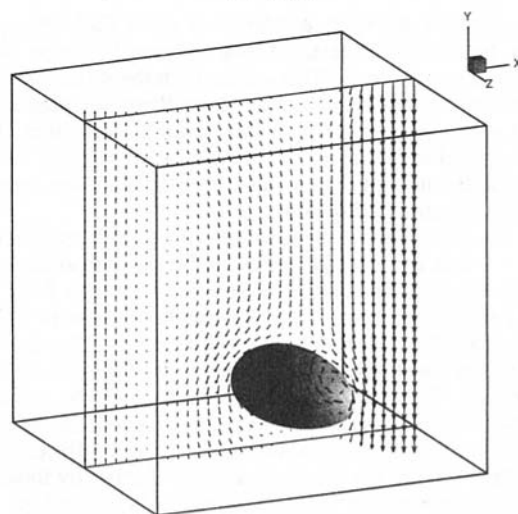


Fig. 10(b)

Fig. 10 Three-dimensional velocity field with respect to the centroid of a steady bubble. $G_R = 16.0$, $Fr^2 = 0.15$, $\eta = 0.025$, $\lambda = 0.10$ and $a/l = 0.15$, $G^*t = 3.6$ and $z/l = 0.5$. (a) $Ca = 0.01$ and initial $x/l = 0.255$. (b) $Ca = 0.07$ and initial $x/l = 0.725$.

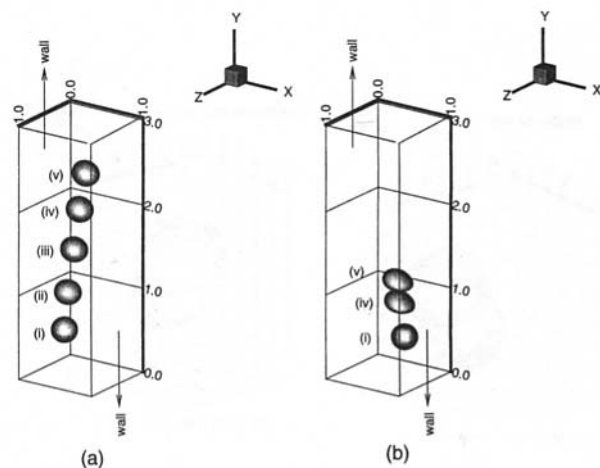


Fig. 9 Motion of a three-dimensional bubble. $G_R = 16.0$, $Fr^2 = 0.15$, $\eta = 0.025$, $\lambda = 0.10$ and $a/l = 0.15$. $G^*t = (i) 0.0$, $(ii) 0.09$, $(iii) 1.8$, $(iv) 2.7$ and $(v) 3.6$. (a) $Ca = 0.01$, (b) $Ca = 0.07$.

similarity between the three-dimensional flow in the center plane and the two-dimensional flow field presented in the previous section suggests that the two-dimensional simulations capture the essential features of the fully three-dimensional results. Figure 10 shows that deformation associated with a higher Ca strengthens the vortex rotating counter to the sheared walls. The strength of the counter rotating vortex is due to the net counter-clockwise circulation around the bubble which determines the net lift, resulting in a bubble that moves in a direction opposite to that of an undeformed bubble (Fig. 9).

Figure 11 depicts the relative bubble velocity in the y -direction (v_{PIF}/U_o), along with Re/G_R . The relative velocity for both bubbles increased rapidly from zero at early times and then slowly began to level. The steady state lift of the fully three-dimensional bubbles has not been examined, as was done for the two-dimensional ones. However, assuming that lift and drag are balanced by the buoyancy force, we can estimate both from the path of the bubbles. Similar analysis on experimentally obtained paths of unsteady bubbles in a vortex has been done by Shridar and Katz (1995), who also estimated the effect of various unsteady terms. Here, the motion of the bubbles is essentially steady state through most of the channel. For the spherical

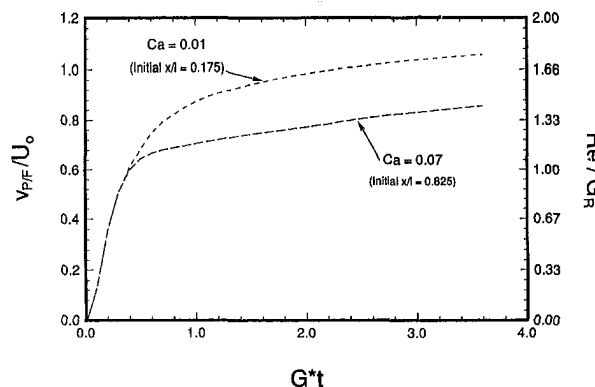


Fig. 11 Bubble rise velocity (v_{PF}/U_o) and Re/G_R as a function of time. $G_R = 16.0$, $Fr^2 = 0.15$, $\eta = 0.025$, $\lambda = 0.10$ and $a/l = 0.15$.

bubble, using the velocities near $G^*t = 3$, when the bubble is in the middle of the channel, the force balance results in:

$$C_{fx} = \frac{2}{3} \left(\frac{G_R}{Fr^*Re} \right)^2 \sin(\theta) = 0.265, \quad (10)$$

where $\theta = 9.93$ deg is the angle between the path and the vertical axis. This can be compared with Shridar and Katz (1995) where the drag coefficient is plotted against the nondimensional shear rate. In their notation, our shear rate is $\alpha = 0.5^*(G_R/Re) = 0.294$, and $C_{fx} = 0.265$ matches their data. While the Reynolds number ($Re = 9.4$) is somewhat lower than those used by Shridar and Katz, their results showed little dependency on the Reynolds number. It is possible that contamination effects were not completely absent in the experiment. The drag coefficient for the spherical bubble, computed in the same way as the lift coefficient, was found to be:

$$C_D = \frac{2}{3} \left(\frac{G_R}{Fr^*Re} \right)^2 \cos(\theta) = 4.54, \quad (11)$$

which is actually slightly higher than what one would expect for a rigid sphere (see Clift, Grace and Weber, 1978). We have, however, neglected all unsteady effects that should be subtracted from the drag force before we find C_D , as well the effects of deformation, finite channel width, and bubble viscosity. All of these can be expected to increase the drag.

Conclusions

Full numerical simulations of deformable buoyant bubbles in a simple vertical shear flow proved satisfactory in that the bubble motions followed previous experimental results. A close examination of the flow characteristics provided a complete explanation of the underlying mechanisms. While spherical bubbles migrated laterally in the same direction as solid spheres, deformable bubbles behaved differently. Buoyancy and shear result in asymmetric deformations that force a circulation around the bubble which opposes the mean shear of the flow. This results in a lift force, F , in a direction opposite to that of solid spherical particles. This mechanism might explain other influences on bubble migration besides gravity, such as non-Newtonian fluids and walls, that also produce asymmetric deformation. A three-dimensional model was used to verify the insights obtained with a two-dimensional model.

The influence of the governing parameters on the resulting lateral lift of a bubble was assessed. Bubbles with a large Ca were more easily distorted, due to the reduction in surface tension, resulting in a lift force controlled by deformation. Increasing G_R and hence the amount of inertia in the flow also increased the deformation and, as a consequence, the negative lift force. Expanding the influence of the gravitational force, by decreasing Fr^2 , also increased the deformation and the deformation induced lift force.

Acknowledgments

This work was supported by the Fluid Dynamics Division of the Office of Naval Research, contract number N00014-91-J-1084, with Dr. E. P. Rood as technical monitor. Some of the calculations were performed at the San Diego Supercomputer center, which is sponsored by the National Science Foundation and some of the calculations were performed at the Ohio Supercomputer center, award number PNS370-2. G. T. would like to thank Professor J. Katz for useful discussions.

References

- Auton, T. R., 1987, "The Lift Force on a Spherical Body in a Rotational Flow," *Journal of Fluid Mechanics*, Vol. 183, pp. 199–218.
- Batchelor, G. K., 1967, *An Introduction to Fluid Dynamics*, Cambridge University Press, Cambridge, Great Britain.
- Bretherton, F. P., 1962, "The Motion of Rigid Particles in a Shear Flow at Low Reynolds Number," *Journal of Fluid Mechanics*, Vol. 14, pp. 284–304.
- Clift, R., Grace, J. R., and Weber, M. E., 1978, *Bubbles, Drops, and Particles*, Academic Press, San Diego, CA.
- Dandy, D. S., and Dwyer, H. A., 1990, "A Sphere in Shear Flow at Finite Reynolds Number: Effect of Shear on Particle Lift, Drag, and Heat Transfer," *Journal of Fluid Mechanics*, Vol. 216, pp. 381–410.
- Ervin, E. A., 1993, "Computations of Bubbles and Drops in Shear Flow," Ph.D. thesis, The University of Michigan, Ann Arbor, MI.
- Goldsmith, H. L., and Mason, S. G., 1962, "The Flow of Suspensions Through Tubes. I. Single Spheres, Rods, and Discs," *Journal of Colloid Science*, Vol. 17, pp. 448–476.
- Kang, I. S., and Leal, L. G., 1989, "Numerical Solution of Axisymmetric, Unsteady Free-Boundary Problems at Finite Reynolds Number. II. Deformation of a Bubble in a Biaxial Straining Flow," *Physics of Fluids A*, Vol. 1, pp. 644–690.
- Kang, I. S., and Leal, L. G., 1987, "Numerical Solution of Axisymmetric, Unsteady Free-boundary Problems at Finite Reynolds Number. I. Finite-Difference Scheme and its Application to the Deformation of a Bubble in a Uniaxial Straining Flow," *Physics of Fluids*, Vol. 30, pp. 1929–1940.
- Karnis, A., and Mason, S. G., 1967, "Particle Motions in Sheared Suspensions. XXIII. Wall Migration of Fluid Drops," *Journal of Colloid Science*, Vol. 24, pp. 164–169.
- Kariyasaki, A., 1987, "Behavior of a Single Gas Bubble in a Liquid Flow with a Linear Velocity Profile," *Proc. of the 1987 ASME-JSME Thermal Engineering Joint Conference*, ASME, New York, NY, pp. 261–267.
- Leal, L. G., 1980, "Particle Motions in a Viscous Fluid," *Annual Review of Fluid Mechanics*, Vol. 12, pp. 435–476.
- McLaughlin, J. B., 1993, "The Lift on a Small Sphere in Wall-Bounded Linear Shear Flows," *Journal of Fluid Mechanics*, Vol. 246, pp. 249–265.
- McLaughlin, J. B., 1991, "Inertial Migration of a Small Sphere in Linear Shear Flows," *Journal of Fluid Mechanics*, Vol. 224, pp. 261–274.
- Rallison, J. M., 1984, "The Deformation of Small Viscous Drops and Bubbles," *Annual Review of Fluid Mechanics*, Vol. 16, pp. 45–66.
- Saffman, P. G., 1965, "The Lift on a Small Sphere in Slow Shear Flow," *Journal of Fluid Mechanics*, Vol. 22, pp. 385–400, and Corrigendum, *Journal of Fluid Mechanics*, Vol. 31 (1968), pp. 624.
- Schlichting, H., 1979, *Boundary-Layer Theory*, 7th edition, McGraw-Hill, New York, NY.
- Sridhar, G., and Katz, J., 1995, "Drag and Forces on Microscopic Bubbles Entrained by a Vortex," *Physics of Fluids*, Vol. 7, pp. 389–399.
- Uijttewaal, W. S. J., Nijhof, E.-J., and Heethaar, R. M., 1993, "Droplet Migration, Deformation, and Orientation in the Presence of a Plane Wall: A Numerical Study Compared with Analytical Theories," *Physics of Fluids A*, Vol. 5, pp. 819–825.
- Unverdi, S. O., and Tryggvason, G., 1992a, "A Front-tracking Method for Viscous, Incompressible, Multi-Fluid Flows," *Journal of Computational Physics*, Vol. 100, pp. 25–37.
- Unverdi, S. O., and Tryggvason, G., 1992b, "Computations of Multi-Fluid Flows," *Physica D*, Vol. 60, pp. 70–83.
- Zhou, H., and Pozrikidis, C., 1993, "The Flow of Suspensions in Channels: Single Files of Drops," *Physics of Fluids A*, Vol. 5, pp. 311–324.